Quantum-nondemolition measurements using cold trapped atoms: Comparison between theory and experiment

Alice Sinatra, Jean-François Roch, Karine Vigneron, Philippe Grelu, Jean-Philippe Poizat, Kaige Wang, Philippe Grangier

Quantum-nondemolition measurements using cold trapped atoms: Comparison between theory and experiment

A. Sinatra,* J. F. Roch, K. Vigneron, Ph. Grelu, J.-Ph. Poizat, Kaige Wang,† and P. Grangier
Institut d'Optique, Boîte Postale 147, F-91403 Orsay Cedex, France
(Received 15 July 1997)

In this paper we present a detailed theoretical analysis of a recent quantum-nondemolition experiment in optics using cold atoms in a magneto-optical trap as a nonlinear medium. A signal beam and a meter beam from two independent lasers are coupled within a Λ-type three-level scheme in the $D1$ line of ^{87}Rb atoms. The experimental results for the relevant quantum correlations of the fields, that represent up to now the best achievements for a single back-action evading measurement, are found in a remarkably good agreement with the theoretical predictions from a fully quantum model for three-level atoms in a doubly resonant cavity. [S1050-2947(98)05203-2]

PACS number(s): 42.50.Lc, 32.80.Pj, 42.50.Dv, 42.65.Pc

I. INTRODUCTION

A. General features

As summed up by the Heisenberg uncertainty relation, noise is introduced into a physical system when a quantum measurement is performed on a given observable. The principle of quantum nondemolition (QND) measurements, which was first introduced theoretically by Braginsky and co-workers [1] and Thorne *et al.* [2], is to overcome this measurement noise by repeatedly ''hiding'' it in another observable which is not of interest. In the case where the noise is entirely kept into an observable which is conjugate with the measured quantity, the measurement is said to be back-Action evading (BAE). Though initially proposed for mechanical oscillators, these ideas were greatly developed, both theoretically and experimentally, in the field of quantum optics.

In particular, quantum measurements performed on propagating laser beams are very good candidates for implementing QND or BAE schemes. The basic idea of these schemes is to couple two light beams, usually called ''signal'' and ''meter'' beams, via an optically nonlinear medium (see Ref. [3] for theoretical proposals). Then, for an appropriately designed coupling, direct or homodyne detection of the meter beam will perform a BAE measurement on the signal beam [4–10]. The nonlinear medium may display either second-order ($\chi^{(2)}$) or third-order ($\chi^{(3)}$) optical nonlinearities. The former have the important advantages of being well understood, and of adding very small excess noise to the interacting light beams; they were used in several successful experiments (see, e.g., Ref. [9] and references therein). On the other hand, the latter ($\chi^{(3)}$) nonlinearities are usually accompanied by significant excess noise from the nonlinear medium, which has been attributed to thermally excited Brillouin scattering in optical fibers [4,7], or to absorption and/or spontaneous emission noise in quasiresonant media [11,6]. Nevertheless the last word about the exploitation of ($\chi^{(3)}$) nonlinearities for quantum nondemolition experiments has not yet been pronounced.

A theoretical analysis done for motionless atoms [12] predicted that it should be possible to obtain almost full control of absorption and spontaneous emission processes, provided that appropriate laser powers and detunings are used. On the other hand, the atomic media used so far, which are atomic beams or vapor cells, also exhibit other types of fluctuations, associated with collisions and/or atomic motion [8]. Atomic motion causes fluctuations in the refractive index due to the fluctuating number of atoms in the interaction region, and thus degrades quantum noise reduction effects. An open way to improve atomic media is then clearly to use a medium of cold trapped atoms [13]; in these media, in fact, the time scale of the fluctuations in the number of interacting particles, characterized by the transit time of the atoms across the interaction region, is about three orders of magnitude slower than in atomic beams or vapor cells. In other words, atom number fluctuations in traps have characteristic frequencies that are typically in the kHz range, and do no affect the noise analysis that is performed in the MHz range (see, for example, Sec. V). Moreover, despite the lower densities usually obtained in traps with respect to atomic beams or vapor cells, the elimination of the Doppler broadening of the atomic lines allows one to control small atomic detunings accurately, and consequently to achieve large nonlinear effects. Though these arguments have only a qualitative character, it will be shown below that, when compared to atomic beam experiments [6,8,14], QND experiments performed with cold atoms do achieve both an improved efficiency and an improved agreement with theoretical models.

B. Motivations of the work

In this article we give a detailed theoretical analysis of a recent experiment [10], where QND measurements are performed using rubidium atoms in a magneto-optical trap (MOT) as a nonlinear medium. Using a Λ-type three-level system in the $D1$ line of ^{87}Rb, the observed performances are quantitatively the best obtained so far for a single back-action-evading measurement. Moreover, the MOT and the

*Permanent address: Istituto Nazionale Fisica della Materia, Dipartimento di Fisica dell'Università, Via Celoria 16, 20133 Milano, Italy.

†Permanent address: Department of Physics, Beijing Normal University, Beijing 100875, China.

QND effect are both running continuously at the same time, and mutual perturbations have been avoided by using different optical transitions and a ''dark-spot'' technique [15]. From the theoretical viewpoint, we extend the analysis done in [12] on QND measurements using three-level atoms in a ghost transition scheme, by including the case in which the fields are not resonant in the cavity. How this scheme can be realized and optimized in a real experiment will be analyzed in detail, by taking explicitly into account the constraints imposed by the optical cavity and by the atomic energy-level configuration.

C. Overview of the paper

In Sec. II we briefly introduce the criteria that were developed to evaluate the efficiency of a real quantum nondemolition device. The model is presented in Sec. III. In Sec. IV we illustrate the configuration used to perform the QND measurement, and show how we can choose the adjustable parameters of our system in order to optimize the QND performances. In Sec. V we present the setup of our experiment. Finally, in Sec. VI we compare the results of the model with the experimental results.

II. CHARACTERIZATION OF A REAL QND MEASUREMENT

A. Introduction

Appropriate criteria for evaluating the efficiency of system as a ''real'' (i.e., nonideal) QND device were discussed in several papers [16,17]. It is now generally admitted that three necessary criteria for BAE operation of a device are given by looking, on the one hand, at its input-output properties, and on the other hand at the quantum correlations established between the signal and meter outputs.

More precisely, we are interested in the small time-dependent quantum fluctuations $\delta X_s(t)$ of the *signal* field *amplitude quadrature* about its steady-state value, defined by the relation:

$$X_s(t)-\langle X_s\rangle_{\rm st}=\delta X_s(t), \tag{1}$$

and we are willing to ''read out'' those fluctuations in the meter field *phase quadrature* fluctuations $\delta Y_s(t)$ about the steady-state value which are defined in the same fashion:

$$Y_m(t)-\langle Y_m\rangle_{\rm st}=\delta Y_m(t). \tag{2}$$

With a larger generality, the signal field amplitude may carry out a small *coherent modulation* $X_s'(t)$, the amplitude and the frequency of the modulation being much smaller than the mean amplitude and the optical frequency of the field, respectively. The steady state of the system is thus ''modulated'' about the stable time independent solution $\langle X_s\rangle_{\rm st}$, $\langle Y_m\rangle_{\rm st}$, and one has

$$X_s(t)-\langle X_s\rangle_{\rm st}=X_s'(t)+\delta X_s(t), \tag{3}$$

$$Y_m(t)-\langle Y_m\rangle_{\rm st}=Y_m'(t)+\delta Y_m(t), \tag{4}$$

where, as in Eqs. (1) and (2), the terms which are kept on the right-hand side are small and will be treated linearly. By regarding the QND device as a black box with two input channels and two output channels represented by the incoming and outcoming signal and meter fields, we are interested in describing how the incoming signal amplitude fluctuations $\delta X_s^{\rm in}(t)$ or modulations $X_s'^{\rm in}(t)$ are transferred to the two output channels of the device represented by the signal and the meter outputs. In an ideal QND device, the incoming fluctuations or modulations of the signal amplitude are left unchanged at the signal output, and they are at the same time perfectly reproduced by the meter output, allowing us to perform an ideally accurate and nondestructive measurement. For real experiments three criteria were developed to quantify the efficiency of a system as a QND device, by taking inspiration from the possible applications of the nondestructive measurements as detailed below.

B. Input-output transfer coefficients and correlations

A first important application of the QND measurement, for example in the field of telecommunications, is related to the possibility of reading an amount of information encoded in a beam without adding noise. Let us assume, for example, that the experimenter gives a classical modulation to the signal amplitude at a certain frequency. We would like to ''read'' the modulation, which represents the information carried by the signal field, without degrading it, thus leaving the information available for other users along the same transmission line.

By restricting ourselves to the linearized regime for quantum fluctuations and coherent modulations, we can consider the QND device as a linear amplifier, and study how the modulation and the noise are transferred from the signal input channel to the signal output and the meter output channels. In the frequency space, by introducing the Fourier transform (denoted with the tilde) of the time dependent quantities defined above, one has

$$\widetilde{X}'^{\rm out}_s(\omega)=g_s\widetilde{X}'^{\rm in}_s(\omega), \tag{5}$$

$$\delta\widetilde{X}^{\rm out}_s(\omega)=g_s\delta\widetilde{X}^{\rm in}_s(\omega)+B^{\rm add}_s(\omega) \tag{6}$$

for the signal output channel, and

$$\widetilde{Y}'^{\rm out}_m(\omega)=g_m\widetilde{X}'^{\rm in}_s(\omega), \tag{7}$$

$$\delta\widetilde{Y}^{\rm out}_m(\omega)=g_m\delta\widetilde{X}^{\rm in}_s(\omega)+B^{\rm add}_m(\omega) \tag{8}$$

for the meter output channel, where g_s and g_m represent the gains of the amplifier in the signal output and in the meter output channel, respectively, which are the same for the signal input noise and the modulation, while $B_s^{\rm add}$ and $B_m^{\rm add}$ represent the extra noises added by the amplifier in the two channels, which could come for example from the atomic noise or from the input meter noise and the signal phase noise $[\delta\widetilde{Y}^{\rm in}_s(\omega)]$ processed by the system. By assuming that the fields injected in the QND device are in a coherent state, we suppose that $B_s^{\rm add}$ and $B_m^{\rm add}$ are not correlated with $\delta\widetilde{X}^{\rm in}_s(\omega)$; a more general treatment was given in Ref. [17]. The signal-to-noise ratio (SNR) for the input channel of the signal field is then defined as the ratio between the intensity of the small classical modulation given to the signal field

amplitude quadrature at a certain frequency and the quantum noise power in the same quadrature at the same frequency:

$$R_s^{\rm in}=\left|\frac{\langle \tilde{X'}_s^{\rm in}(\omega)\rangle^2}{\langle \delta\tilde{X}_s^{\rm in}(\omega)^2\rangle}\right|, \tag{9}$$

and the same quantity can be defined for the two output channels:

$$R_s^{\rm out}=\left|\frac{\langle \tilde{X'}_s^{\rm out}(\omega)\rangle^2}{\langle \delta\tilde{X}_s^{\rm out}(\omega)^2\rangle}\right| \quad \text{and} \quad R_m^{\rm out}=\left|\frac{\langle \tilde{Y'}_m^{\rm out}(\omega)\rangle^2}{\langle \delta\tilde{Y}_m^{\rm out}(\omega)^2\rangle}\right|. \tag{10}$$

One can then define two quantities T_s and T_m, which describe how the incoming SNR (9) is transmitted to two output channels of the QND device:

$$T_s=\frac{R_s^{\rm out}}{R_s^{\rm in}} \quad \text{and} \quad T_m=\frac{R_m^{\rm out}}{R_s^{\rm in}}. \tag{11}$$

From Eqs. (5)–(8), one has

$$T_s=\frac{\langle \delta\tilde{X}_s^{\rm in}(\omega)^2\rangle}{\langle \delta\tilde{X}_s^{\rm in}(\omega)^2\rangle+\langle[\delta B_s^{\rm add}(\omega)/g_s]^2\rangle} \quad \text{and}$$

$$T_m=\frac{\langle \delta\tilde{X}_s^{\rm in}(\omega)^2\rangle}{\langle \delta\tilde{X}_s^{\rm in}(\omega)^2\rangle+\langle[\delta B_m^{\rm add}(\omega)/g_m]^2\rangle}. \tag{12}$$

The coefficient T_s evaluates to what extent the measurement is nondestructive, i.e., how the signal-to-noise ratio is degraded after the measurement: $T_s=1$ for an ideal nondestructive measurement, while $T_s=0$ if the measurement is totally destructive. Similarly, T_m evaluates the efficiency of the measurement: a perfectly accurate measurement would correspond to $T_m=1$, while $T_m=0$ if no information is gained. For achieving QND performances, one requires that $T_s+T_m>1$, which can be obtained only by using a phase-sensitive device. On the other hand, $T_s+T_m=1$ is the performance of a simple beam splitter [17]. These transfer coefficients are very useful because they are directly accessible in an experiment. The SNR values can indeed be visualized very easily on a spectrum analyzer, and it is then straightforward to measure the various SNR and to work out the transfer coefficients.

From a formal point of view, it is also possible to consider the normalized correlations between the meter or signal output and the signal input quantum fluctuations, which were first introduced by Holland *et al.* in Ref. [16], and which we will calculate theoretically. Precisely one defines

$$C_s=\frac{|\langle \delta X_s^{\rm in}\delta X_s^{\rm out}\rangle_\omega|^2}{\langle \delta X_s^{\rm in}\delta X_s^{\rm in}\rangle_\omega\langle \delta X_s^{\rm out}\delta X_s^{\rm out}\rangle_\omega},$$

$$C_m=\frac{|\langle \delta X_s^{\rm in}\delta Y_m^{\rm out}\rangle_\omega|^2}{\langle \delta X_s^{\rm in}\delta X_s^{\rm in}\rangle_\omega\langle \delta Y_m^{\rm out}\delta Y_m^{\rm out}\rangle_\omega}, \tag{13}$$

where $\langle AB\rangle_\omega$ denotes the Fourier transform of the symmetrized correlation function between the two operators in brackets:

$$\langle AB\rangle_\omega=\int_{-\infty}^{+\infty}e^{-i\omega t}\langle A(t)B\rangle_{\rm sym}dt \quad \text{with}$$

$$\langle A(t)B\rangle_{\rm sym}=\langle A(t)B+BA(t)\rangle/2. \tag{14}$$

Contrary to the previous ones, these quantities cannot be measured directly in a single BAE experiment, because the input fluctuations are not known in advance. However, it can be shown that in the linearized regime for fluctuations and small modulations, and for coherent input states of the fields into the QND device, one simply has

$$C_s=T_s \quad \text{and} \quad C_m=T_m, \tag{15}$$

and the correlation coefficients can be therefore calculated and used as the transfer coefficients; we emphasize, however, that this is not generally true when the input beam has phase-dependent excess noise, in which case some precautions are required [17].

C. Conditional variance

A second application of the QND measurement concerns the situation where we are interested directly in the quantum fluctuations of the fields. If the intensity fluctuations of an incoming beam are measured in a nondestructive way, the acquired information can be used, at the output of the QND device, to correct the signal beam by reducing its fluctuations. The third QND criterion, relative to this application, is given by the output conditional variance of the signal field, given the result of a measurement on the meter field:

$$V_{s|m}=\langle \delta X_s^{\rm out}\delta X_s^{\rm out}\rangle_\omega(1-C_{\rm sm}), \tag{16}$$

where $C_{\rm sm}$ is a normalized correlation between the meter and the signal outputs,

$$C_{\rm sm}=\frac{|\langle \delta X_s^{\rm out}\delta Y_m^{\rm out}\rangle_\omega|^2}{\langle \delta X_s^{\rm out}\delta X_s^{\rm out}\rangle_\omega\langle \delta Y_m^{\rm out}\delta Y_m^{\rm out}\rangle_\omega}, \tag{17}$$

and where $\langle AB\rangle_\omega$ is defined as in Eq. (14).

For an ideal QND device, $C_{\rm sm}=1$ and $V_{s|m}=0$, while in a real device one requires that the information gained by the measurement is sufficient to reduce the intensity fluctuation of the initial beam under the shot-noise level, corresponding to $V_{s|m}<1$.

In a QND experiment, the signal noise reduction is usually not implemented, and the conditional variance $V_{s|m}$ is measured electronically by subtracting the photocurrent of the meter readout $Y_m^{\rm out}$ from the photocurrent of the outgoing signal $X_s^{\rm out}$, with an appropriate gain or attenuation. More precisely, the quantum fluctuations of these recombined currents will be given by the spectral variance of $(X_s^{\rm out}-gY_m^{\rm out})$, where g is an electronic gain or attenuation. In the ideal case, the meter beam will reproduce the actual noise of the output signal beam up to a multiplicative factor, and it will be possible to correct exactly the signal noise by bringing the variance of $(X_s^{\rm out}-gY_m^{\rm out})$ to zero. In the general case, the variance of $(X_s^{\rm out}-gY_m^{\rm out})$ is

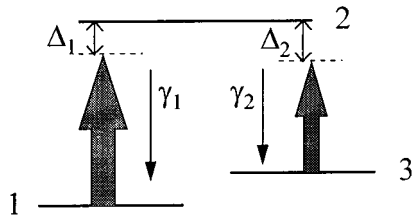

FIG. 1. Energy-level scheme of the Λ three-level atoms.

$$V_{s|m}^{(g)}=\langle \delta X_s^{\rm out}\delta X_s^{\rm out}\rangle_\omega+|g|^2\langle \delta Y_m^{\rm out}\delta Y_m^{\rm out}\rangle_\omega - 2\,{\rm Re}(g\langle \delta X_s^{\rm out}\delta Y_m^{\rm out}\rangle_\omega); \tag{18}$$

the minimum value of this quantity is obtained by choosing

$$g=\langle \delta X_s^{\rm out}\delta Y_m^{\rm out}\rangle_\omega^*/\langle \delta Y_m^{\rm out}\delta Y_m^{\rm out}\rangle_\omega, \tag{19}$$

for which choice one has in fact

$$V_{s|m}^{(g)}=V_{s|m}, \tag{20}$$

with $V_{s|m}$ given by Eq. (16). In a real experimental situation, the amplitude and phase of the g factor are adjusted using an attenuator and a delay line in order to minimize the photocurrent difference. The minimum noise level obtained using this procedure gives the value of $V_{s|m}$.

III. MODEL

A. Equations

We consider a three-level atomic medium at rest, inside an optical ring cavity; $\mathcal{L}$ is the roundtrip length of the cavity, occupied by the medium for a length L. Two laser fields of carrier frequencies ω_1 and ω_2 are injected in the cavity; the fields are supposed to be close to resonance with two atomic transitions frequencies ω_r and ω_s, and with two cavity eigenfrequencies ω_{c1} and ω_{c2}. The cavity is single ended for each field, T_i ($i=1$ and 2) being the transmissivity of the coupling mirror. We introduce the decay constants of the fields amplitudes inside the empty (lossless) cavity:

$$\kappa_1=\frac{cT_1}{2\mathcal{L}},\quad \kappa_2=\frac{cT_2}{2\mathcal{L}}, \tag{21}$$

where c is the speed of light in vacuum, and the normalized empty cavity detunings:

$$\theta_1=\frac{\omega_{c1}-\omega_1}{\kappa_1},\quad \theta_2=\frac{\omega_{c2}-\omega_2}{\kappa_2}. \tag{22}$$

The atoms are described as sets of three energy levels disposed in a lambda configuration (Fig. 1). By γ_1 and γ_2 we denote the decay rate constants of the atomic population from the excited level $|2\rangle$ towards levels $|1\rangle$ and $|3\rangle$, respectively, while γ_w, defined as half of the total population decay rate from the upper level,

$$\gamma_w=\frac{\gamma_1+\gamma_2}{2}, \tag{23}$$

is the decay rate constant of the atomic polarizations 1-2 and 3-2 in the radiative limit. We define Δ_1 and Δ_2 the normalized atomic detunings:

$$\Delta_1=\frac{\omega_r-\omega_1}{\gamma_w},\quad \Delta_2=\frac{\omega_s-\omega_2}{\gamma_w}; \tag{24}$$

please note that with definitions (24) positive detunings are red detunings ($\omega_{\rm atom}<\omega_{\rm laser}$). The operators describing the atoms are the polarization operators: σ_{12}, σ_{13}, and σ_{23} obeying the commutation rules

$$[\sigma_{ij},\sigma_{kl}]=\delta_{jk}\sigma_{il}-\delta_{li}\sigma_{kj},\quad i,j=1,2,3, \tag{25}$$

where the δ_{ij} are Kronecker deltas, and the population inversions: $r_3=1/2(\sigma_{22}-\sigma_{11})$ and $s_3=1/2(\sigma_{22}-\sigma_{33})$. The resonant cavity modes are described by the usual boson creation and annihilation operators $a_i^\dagger$ and a_i ($i=1$ and 2), with

$$[a_i,a_i^\dagger]=1,\quad i,j=1,2. \tag{26}$$

The evolution of the system is governed by a master equation for the system density operator ρ, which, in the interaction picture, has the form

$$\frac{\partial\rho}{\partial t}=[-i(L_a+L_f+L_{\rm ext}+L_{\rm af})+\Lambda_a+\Lambda_f]\rho, \tag{27}$$

where

$$L_a\rho=\tfrac{2}{3}\{(2\omega_r-\omega_s)[R_3,\rho]+(2\omega_s-\omega_r)[S_3,\rho]\},$$

$$L_f\rho=(\omega_{c1}-\omega_1)[a_1^\dagger a_1,\rho]+(\omega_{c2}-\omega_2)[a_2^\dagger a_2,\rho],$$

$$L_{\rm ext}\rho=i\{\kappa_1[(\varepsilon_1 a_1^\dagger-\varepsilon_1^* a_1),\rho]+\kappa_2[(\varepsilon_2 a_2^\dagger-\varepsilon_2^* a_2),\rho]\},$$

$$L_{\rm af}\rho=i\{g_1[(a_1^\dagger R^- - a_1 R^+),\rho]+g_2[(a_2^\dagger S^- - a_2 S^+),\rho]\},$$

$$\Lambda_a\rho=\sum_{n=1}^{N}\frac{\gamma_1}{2}([\sigma_{12}^n\rho,\sigma_{21}^n]+[\sigma_{12}^n,\rho\sigma_{21}^n]) + \frac{\gamma_2}{2}([\sigma_{23}^n\rho,\sigma_{32}^n]+[\sigma_{23}^n,\rho\sigma_{32}^n]),$$

$$\lambda_f\rho=\kappa_1\{[a_1\rho,a_1^\dagger]+[a_1,\rho a_1^\dagger]\}+\kappa_2\{[a_2\rho,a_2^\dagger]+[a_2,\rho a_2^\dagger]\}.$$

In this master equation we introduced the collective atomic operators R^+, R^-, S^+, S^-, T^+, T^-, R_3, and S_3 constructed from the single-atom operators σ_{21}^n, σ_{12}^n, σ_{32}^n, σ_{23}^n, σ_{31}^n, σ_{13}^n, r_3^n, and s_3^n, respectively, as described in Ref. [18], and obeying the same commutation rules. The term $L_a\rho$ describes the free evolution of the atoms according to the single-atom Schrödinger Hamiltonian

$$H_a=\tfrac{2}{3}\hbar[r_3(2\omega_r-\omega_s)+s_3(2\omega_s-\omega_r)], \tag{28}$$

where we have conveniently defined the energy of level $|2\rangle$ as $E_{|2\rangle}=\hbar(\omega_s+\omega_r)/3$ in order to get rid of constant factors. Similarly, $L_f\rho$ describes the free evolution of the two cavity modes and $L_{\rm ext}\rho$ accounts for the driving fields ε_1 and ε_2 injected in the cavity. The interaction term $L_{af}\rho$ describes the coupling between fields and atoms, which is written in

the dipole and rotating-wave approximations, g_1 and g_2 being the coupling constants for the transitions 1-2 and 3-2, respectively. The non-Hamiltonian term $\Lambda_a\rho$ accounts for the decay of the atomic polarizations and population inversions (N is the number of atoms), while $\Lambda_f\rho$ accounts for the decay of the intracavity fields due to the escape of photons from the semireflecting cavity mirrors. For simplicity, here we neglect the contributions due to collisions to the decay of the atomic polarization, restricting ourselves to the radiative limit.

By introducing the normalized classical variables, representing mean values of the atomic operators,

$$v=-\frac{\sqrt{2}}{N}\langle R^-\rangle,\quad w=-\frac{\sqrt{2}}{N}\langle S^-\rangle,\quad z=-\frac{1}{N}\langle T^-\rangle,$$

$$m=-\frac{2}{N}\langle R_3\rangle,\quad n=-\frac{2}{N}\langle S_3\rangle, \tag{29}$$

and the normalized Rabi frequencies proportional to the intracavity and input fields E_i and $E_i^{\rm in}$ ($i=1$ and 2),

$$x_i=\frac{\sqrt{2}g_i}{\gamma w}E_i\quad\text{with}\quad E_i=\langle a_i\rangle\quad(i=1,2),$$

$$y_i=\frac{\sqrt{2}q_i}{\gamma_w}\frac{2}{\sqrt{T_i}}E_i^{\rm in}\quad\text{with}\quad E_i^{\rm in}=\varepsilon_i\frac{\sqrt{T_i}}{2}\quad(i=1,2), \tag{30}$$

the semiclassical equations for the normalized variables read

$$\dot{x}_1=-\kappa_1[(1+i\theta_1)x_1-y_1+2C_1v], \tag{31}$$

$$\dot{x}_2=-\kappa_2[(1+i\theta_2)x_2-y_2+2C_2w], \tag{32}$$

$$\dot{v}=-\gamma_w[(1+i\Delta_1)v-x_1m+x_2z], \tag{33}$$

$$\dot{w}=-\gamma_w[(1+i\Delta_2)w-x_2n+x_1z^*], \tag{34}$$

$$\dot{z}=-\gamma_w\left[i(\Delta_1-\Delta_2)z-\frac{1}{2}(x_1w^*+x_2^*v)\right], \tag{35}$$

$$\dot{m}=-\gamma_1\left[\frac{1}{3}(\eta+2)(m+n-1)+\frac{\gamma_w}{\gamma_1}(x_1v^*+x_1^*v)+\frac{\gamma_w}{2\gamma_1}(x_2w^*+x_2^*w)\right], \tag{36}$$

$$\dot{n}=-\gamma_1\left[\frac{1}{3}(1+2\eta)(m+n-1)+\frac{\gamma_w}{2\gamma_1}(x_1v^*+x_1^*v)+\frac{\gamma_w}{\gamma_1}(x_2w^*+x_2^*w)\right], \tag{37}$$

where we have introduced the ratio $\eta=\gamma_2/\gamma_1$ and the cooperativity parameters

$$C_1=\frac{g_1^2N}{2\kappa_1\gamma_w},\quad C_2=\frac{g_2^2N}{2\kappa_2\gamma_w} \tag{38}$$

proportional to the number of atoms that characterize the strength of the coupling between atoms and the two fields.

B. Steady state

Due to the high degree of symmetry of the equations for the lambda system, it is possible to calculate analytically the steady-state solution for the mean values of the atomic operators (29) and the intracavity fields x_1 and x_2, as a function of the input fields intensities and the remaining system parameters.

In the following we give the exact analytical solution for the intracavity fields in the general case for the system parameters. The steady-state mean values are calculated by solving the system of nonlinear equations obtained by setting the right-hand sides of Eqs. (31)–(37) to zero.

By suitable redefinition of the phases of the polarization variables and of the input fields, it is possible have the intracavity fields x_1 and x_2 real numbers at steady state. In particular we introduce the new variables $\tilde{v}=ve^{-i\phi_1^s}$, $\tilde{w}=we^{-i\phi_2^s}$, $\tilde{z}=ze^{-i(\phi_1^s-\phi_2^s)}$, $\tilde{y}_i=y_ie^{-i\phi_i^s}$, and $\tilde{x}_i=|x_i|$ ($i=1$ and 2), where ϕ_i ($i=1$ and 2) is the phase of the ith field at steady state. We shall use these variables in the following, although we omit the ''tildes'' for typing convenience.

1. Solution in the general case

As we said, it is possible to solve exactly the Bloch equations (33)–(37) at steady state, finding the analytical dependence of the atomic variables on the fields variables (x_1,x_2) and system parameters. By substituting the solutions of the Bloch equations in Eqs. (31) and (32) at steady state, one obtains the solutions for the fields, which read

$$x_1^2=\frac{|y_1|^2}{[1+2C_1b^2I_2\Pi]^2+[\theta_1+2C_1bI_2(\eta I_1+I_2-b\Delta_1)\Pi]^2}, \tag{39}$$

$$x_2^2=\frac{|y_2|^2}{[1+2C_2b^2\eta I_1\Pi]^2+[\theta_2-2C_2bI_1(\eta I_1+I_2+b\eta\Delta_2)\Pi]^2}, \tag{40}$$

where we have defined

$$\gamma=2\frac{\gamma_w}{\gamma_1},\quad I_1=x_1^2,\quad I_2=x_2^2,\quad b=2(\Delta_1-\Delta_2),\quad (41)$$

and where

$$\Pi=\Big\{\eta I_1^3+I_2^3+(2\eta+1)I_1^2I_2+(\eta+2)I_1I_2^2+2b\Delta_2\eta I_1^2 -2b\Delta_1I_2^2+b\left[\frac{3}{2}\gamma b+(1+\eta)(\Delta_2-\Delta_1)\right]I_1I_2+b^2\eta(\Delta_2^2+1)I_1+b^2(\Delta_1^2+1)I_2\Big\}^{-1}. \quad (42)$$

2. Phases of the input and output fields

Let us consider Eqs. (31) and (32) at the steady state; from Eq. (30), one has

$$E_1^{\rm in}=M_1[(1+i\theta_1)x_1+2C_1v], \quad (43)$$

$$E_2^{\rm in}=M_2[(1+i\theta_2)x_2+2C_2w], \quad (44)$$

where $M_i=(\gamma_w\sqrt{T_i})(2\sqrt{2}g_i)^{-1}$ are proportionality constants. The phases $\Theta_1^{\rm in}$ and $\Theta_2^{\rm in}$ of the input fields are then calculated as $\Theta_1^{\rm in}=\arctan[{\rm Im}(E_i^{\rm in})/{\rm Re}(E_i^{\rm in})]$ for ($i=1$ and 2). By using Eqs. (30), (43), and (44), and the boundary condition for our single-port cavity,

$$E_i^{\rm out}+E_i^{\rm in}=\sqrt{T_i}E_i\quad (i=1,2), \quad (45)$$

one has

$$E_1^{\rm out}=-M_1[(-1+i\theta_1)x_1+2C_1v], \quad (46)$$

$$E_2^{\rm out}=-M_2[(-1+i\theta_2)x_2+2C_2w], \quad (47)$$

from which the phases the phases $\Theta_1^{\rm out}$ and $\Theta_2^{\rm out}$ of the output fields are calculated in the same way.

3. Double-resonance condition

By using the steady-state solutions (39) and (40), we may easily find the condition in which both fields are resonant in the cavity at the same time. This situation is particularly favorable for the QND experiment [12], and it can be expressed as a precise requirement on the cavity detunings and input fields amplitudes, given certain values of the intracavity fields intensities I_1, and I_2, and atomic detunings Δ_1 and Δ_2. Such requirements read

$$\theta_1=-2C_1bI_2(\eta I_1+I_2-b\Delta_1)\Pi, \quad (48)$$

$$\theta_2=2C_2bI_1(\eta I_1+I_2+b\eta\Delta_2)\Pi, \quad (49)$$

$$|y_1|=\sqrt{I_1}(1+2C_1b^2I_2\Pi), \quad (50)$$

$$|y_2|=\sqrt{I_2}(1+2C_2b^2\eta I_1\Pi). \quad (51)$$

It should be noted that, in practice, it will not be trivial to realize the double-resonance condition for a given cavity and for a given atomic system. On the one hand, the choice of the laser frequencies fixes the cavity and atomic detunings, and, on the other hand, for the fields to be resonant, these quantities have to linked by relations (48) and (49). This constraint will be discussed below.

C. Constraint on the detunings

We think it is worth considering in some detail how the double-resonance conditions (48)–(51) can be achieved in an experiment; to this aim, we introduce the normalized detunings

$$\Delta_A=\frac{\omega_r-\omega_s}{\gamma_w},\quad \Delta_C=\frac{\omega_{c1}-\omega_{c2}}{\kappa_1}, \quad (52)$$

representing the distance in frequency between the two lower atomic levels and between the two cavity eigenfrequencies nearly resonant with the input fields, respectively. We point out that, due to its normalization, Δ_C does not depend on the cavity length. By construction, a relation holds between the cavity and the atomic detunings introduced so far:

$$\theta_1=\left(\frac{\kappa_2}{\kappa_1}\right)\theta_2=(\Delta_1-\Delta_2-\Delta_A)\frac{\gamma_w}{\kappa_1}+\Delta_C. \quad (53)$$

Equation (53) tells us that once the distance in frequency between the two lasers is fixed, for example, by our choice of the atomic detunings, the difference between the cavity detunings is automatically fixed by the properties of the cavity through Δ_C, κ_1, and κ_2. On the other hand, if we need both fields at resonance in the cavity, the cavity detunings should compensate for the phase shifts introduced by the atoms, which impose that:

$$\theta_1-\left(\frac{\kappa_2}{\kappa_1}\right)\theta_2=F(C_1,C_2,I_1,I_2,\Delta_1,\Delta_2), \quad (54)$$

where F is a function of the indicated parameters which is obtained easily from Eq. (48) and (49). Equations (53) and (54) represent thus two independent requirements on the quantity $\theta_1-(\kappa_2/\kappa_1)\theta_2$ which should be fulfilled at the same time. In particular, the right-hand sides of Eqs. (53) and (54) should be equal, which constraints, for a given cavity and a given medium, the possible values of the atomic detunings and intracavity fields for which the double-resonance condition can be achieved.

We will return to this constraint on parameters in Sec. IV B by considering in particular the case of our experimental setup and the mean fields configuration that we use to perform the QND measurements. Before this, however, we would like to go back to Eq. (53) and make some further remarks. Equation (53) is a relation between the cavity and the atomic detunings that is automatically fulfilled in a real experiment, suggesting that the four parameters of our model should not be considered as independent. In order to evaluate the significance of this relation in the different experimental situations, we rewrite Eq. (53) as

$$\theta_1-\left(\frac{\kappa_2}{\kappa_1}\right)\theta_2=\frac{4\pi}{T_1}\left(\frac{1}{\lambda_2}-\frac{1}{\lambda_1}\right)\mathcal{L}+\Delta_C, \tag{55}$$

where we used Eqs. (21), (24), and (52). Now several situations are possible. Suppose first that the frequencies ω_1 and ω_2 of the input fields are well separated on the optical-frequency scale (as, for example, in the experiments described in Refs. [6, 8]). Equation (55) shows that extremely small adjustments of the cavity length $\mathcal{L}$, on the order of $1/[(1/\lambda_1)-(1/\lambda_2)]\sim\lambda$, are in this case sufficient to adjust at will the difference $\theta_1-(\kappa_2/\kappa_1)\theta_2$ once the two laser frequencies have already been fixed. In such conditions, atomic and cavity detunings can in fact be considered as independent parameters; and in particular the double-resonance conditions (48) and (49) can be realized without any restriction on the atomic detunings Δ_1 and Δ_2. Let us now consider the opposite case in which the two frequencies ω_1 and ω_2 are very close one another. This could be, for example, the case when the two ground levels of the lambda scheme are degenerate Zeeman sublevels. If ω_1 and ω_2 are only a few MHz apart, adjustments of the cavity length on the order of the *meter* (that is of course out of reach in an experiment) would be necessary in order to change the difference $\theta_1-(\kappa_2/\kappa_1)\theta_2$ by some units when the laser frequencies have already been fixed. In this case Eq. (53) represents a serious constraint that cannot be overcome by adjustments of the cavity length. In between the two limiting cases considered above, there are situations in which, if on the one hand Eq. (53) represents a real constraint, still some room is left for small adjustments of the cavity detunings by significant changes of $\mathcal{L}$. A similar situation is encountered in the experiment with cold atoms that we consider in detail in this paper (Sec. V), where the two ground levels of the lambda scheme are hyperfine sublevels 6.83 GHz apart.

D. Quantum noise analysis

In order to calculate the QND coefficients defined in Sec. II, we are interested in the time-dependent correlation functions of the fields whose amplitude and phase fluctuate around a steady-state mean value. We consider the case in which the the fluctuations are small with respect to the mean values and a linearized treatment of the fluctuations is possible. Let Ξ_i^{ϕ} be a certain quadrature of the ith field ($i=1$ and 2), relative to the reference phase ϕ:

$$\Xi_i^{\phi}=a_i e^{-i\phi}+a_i^{\dagger}e^{i\phi}. \tag{56}$$

In the notations of Sec. II, and referring to the phases of the input and output fields at steady state introduced in Sec. III B, one has

$$\delta X_s^{\rm in}=\delta\Xi_2^{\Theta_2^{\rm in}} \quad \delta X_s^{\rm out}=\delta\Xi_2^{\Theta_2^{\rm out}}$$

$$\delta Y_m^{\rm in}=\delta\Xi_1^{\Theta_1^{\rm in}(\pi/2)} \quad \delta Y_m^{\rm out}=\delta\Xi_1^{\Theta_1^{\rm out}+(\pi/2)} \tag{57}$$

where by $\delta\Xi_i^{\phi}$ we denote the time-dependent fluctuation of the operator Ξ_i^{ϕ} around a steady-state point in the Heisenberg picture:

$$\delta\Xi_i^{\phi}=\delta a_i e^{-i\phi}+\delta a_i^{\dagger}e^{i\phi}, \quad \text{with} \quad \delta a_i=a_i-\langle a_i\rangle \quad (i=1,2). \tag{58}$$

By using the the input-output relations [19]

$$a_i^{\rm out}+a_i^{\rm in}=\sqrt{2\kappa_i}a_i \quad (i=1 \quad \text{and} \quad 2), \tag{59}$$

whose classical counterpart is represented by Eq. (45), and assuming that the input fields are in a coherent state, one obtains

$$\begin{aligned}\langle \delta X_s^{\rm in}(t)\,\delta Y_m^{\rm out}\rangle_{\rm sym}=i\sqrt{\kappa_1\kappa_2}\;\Theta(t)\big[&\langle[\alpha_1^{\dagger}(t),\alpha_2]\rangle e^{i(\Theta_1^{\rm out}-\Theta_2^{\rm in})}\\&-\langle[\alpha_1^{\dagger}(t),\alpha_2^{\dagger}]\rangle e^{i(\Theta_1^{\rm out}+\Theta_1^{\rm in})}\\&-\langle[\alpha_1(t),\alpha_2]\rangle e^{-i(\Theta_1^{\rm out}+\Theta_2^{\rm in})}\\&+\langle[\alpha_1(t),\alpha_2^{\dagger}]\rangle e^{-i(\Theta_1^{\rm out}-\Theta_2^{\rm in})}\big],\end{aligned} \tag{60}$$

$$\begin{aligned}\langle \delta X_s^{\rm in}(t)\,\delta X_s^{\rm out}\rangle_{\rm sym}=\kappa_2\Theta(t)\big[&-\langle[\alpha_2(t),\alpha_2]\rangle e^{-i(\Theta_2^{\rm out}+\Theta_2^{\rm in})}\\&+\langle[\alpha_2^{\dagger}(t),\alpha_2^{\dagger}]\rangle e^{i(\Theta_2^{\rm out}+\Theta_2^{\rm in})}\\&+\langle[\alpha_2^{\dagger}(t),\alpha_2]\rangle e^{-i(\Theta_2^{\rm out}-\Theta_2^{\rm in})}\\&-\langle[\alpha_2(t),\alpha_2^{\dagger}]\rangle e^{i(\Theta_2^{\rm out}-\Theta_2^{\rm in})}\big]\\&-\delta(t)\cos(\Theta_2^{\rm out}-\Theta_2^{\rm in}),\end{aligned} \tag{61}$$

$$\begin{aligned}\langle \delta X_s^{\rm out}(t)\,\delta Y_m^{\rm out}\rangle_{\rm sym}=-2i\sqrt{\kappa_1\kappa_2}\big[&-\langle:\alpha_1(t)\alpha_2:\rangle\\&\times e^{-i(\Theta_1^{\rm out}+\Theta_2^{\rm out})}+\langle:\alpha_1^{\dagger}(t)\alpha_2:\rangle\\&\times e^{i(\Theta_1^{\rm out}-\Theta_2^{\rm out})}-\langle:\alpha_1(t)\alpha_2^{\dagger}:\rangle\\&\times e^{-i(\Theta_1^{\rm out}-\Theta_2^{\rm out})}+\langle:\alpha_1(t)^{\dagger}\alpha_2^{\dagger}:\rangle\\&\times e^{i(\Theta_1^{\rm out}+\Theta_2^{\rm out})}\big],\end{aligned} \tag{62}$$

where the dots in Eq. (62) mean time and normal ordering:

$$\langle:\alpha_i(t)\alpha_j^{\dagger}:\rangle=\langle\alpha_j^{\dagger}\alpha_i(t)\rangle,$$

$$\langle:\alpha_i(t)^{\dagger}\alpha_j:\rangle=\langle\alpha_i(t)^{\dagger}\alpha_j\rangle,$$

$$\langle:\alpha_i(t)\alpha_j:\rangle=\Theta(-t)\langle\alpha_j\alpha_i(t)\rangle+\Theta(t)\langle\alpha_i(t)\alpha_j\rangle,$$

$$\langle:\alpha_i(t)^{\dagger}\alpha_j^{\dagger}:\rangle=\Theta(-t)\langle\alpha_i(t^{\dagger})\alpha_i^{\dagger}\rangle+\Theta(t)\langle\alpha_j^{\dagger}\alpha_i(t)^{\dagger}\rangle,$$

where $\Theta(t)$ is the step-function taking the values 1, $\frac{1}{2}$ or 0, when t is larger than, equal to, or smaller than zero, respectively, and where for brevity we have introduced the notation

$$\alpha_i=\delta a_i=a_i-\langle a_i\rangle \quad (i=1 \quad \text{and} \quad 2). \tag{63}$$

By taking the Fourier transforms of the symmetrized correlations (60)–(62), we are eventually concerned with the calculation of response functions

$$R_{jk}(\omega)=\int_{-\infty}^{+\infty}\Theta(\tau)\langle[\beta_j(\tau),\beta_k]\rangle e^{-i\omega\tau}d\tau \quad (j,k=1,2,3,4). \tag{64}$$

and normally ordered correlation functions

$$S_{jk}(\omega)=\int_{-\infty}^{\infty}\langle:\beta_j(\tau)\beta_k:\rangle e^{-i\omega\tau}d\tau, \quad (j,k=1,2,3,4), \tag{65}$$

where we have introduced the vector β_j ($j=1$ and 12) of system operator fluctuations:

$$\vec{\beta}=[\alpha_1,\alpha_1^{\dagger},\alpha_2,\alpha_2^{\dagger},\delta R^-,\delta R^+,\delta S^-,\delta S^+,\delta T^-,\delta T^+,\delta R_3,\delta S_3]^T. \tag{66}$$

In the linearized regime Eqs. (64) and (65) can be easily calculated by using the master equation. We carefully checked that our method, relying on the master equation formalism and the quantum regression theorem [20], gives results identical to the method based on linear-response theory in the frequency domain developed by Courty and Grangier [21], and with the method using the input-output formalism of Collett and Gardiner in the time domain [19,12]. The result for the response functions is

$$R_{jk}(\omega)=[(A+i\omega I)^{-1}C^0]_{jk}, \tag{67}$$

where A is the (12×12) drift matrix obtained linearizing Eqs. (31)–(37) [and the complex conjugates of Eqs. (31)–(35)], and C^0 is the matrix of the equal-time commutators, i.e.,

$$C_{ij}^0=\langle[\beta_i,\beta_j|]\rangle. \tag{68}$$

For the normally ordered correlation functions, one has, instead

$$S_{jk}(\omega)=[(A+i\omega I)^{-1}D_N(A^T-i\omega I)^{-1}]_{jk}, \tag{69}$$

where D_N is the normally ordered diffusion matrix that we report for completeness in the Appendix. The results for the interesting correlations between input and output fields are

$$\begin{aligned}\langle\delta X_s^{\rm in}\delta Y_m^{\rm out}\rangle_\omega=i\sqrt{\kappa_1\kappa_2}[&R_{23}e^{i(\Theta_i^{\rm out}-\Theta_2^{\rm in})}-R_{24}e^{i(\Theta_1^{\rm out}+\Theta_2^{\rm in})}\\&-R_{13}e^{-i(\Theta_1^{\rm out}+\Theta_2^{\rm in})}+R_{14}e^{-i(\Theta_1^{\rm out}-\Theta_2^{\rm in})}],\end{aligned} \tag{70}$$

$$\begin{aligned}\langle\delta X_s^{\rm in}\delta X_s^{\rm out}\rangle_\omega=&-\cos(\Theta_2^{\rm out}-\Theta_2^{\rm in})+\kappa_2[-R_{33}e^{-i(\Theta_2^{\rm out}+\Theta_2^{\rm in})}\\&+R_{44}e^{i(\Theta_{2\rm out}+\Theta_2^{\rm in})}+R_{34}e^{-i(\Theta_2^{\rm out}-\Theta_2^{\rm in})}\\&-R_{43}e^{i(\Theta_2^{\rm out}-\Theta_2^{\rm in})}].\end{aligned} \tag{71}$$

The useful correlations involving only the output fields are instead

$$\begin{aligned}\langle\delta X_s^{\rm out}\delta Y_m^{\rm out}\rangle_\omega=&-2i\sqrt{\kappa_1\kappa_2}[-S_{13}e^{-i(\Theta_1^{\rm out}+\Theta_2^{\rm out})}\\&+S_{23}e^{i(\Theta_1^{\rm out}-\Theta_2^{\rm out})}-S_{14}e^{-i(\Theta_1^{\rm out}-\Theta_2^{\rm out})}\\&+S_{24}e^{i(\Theta_1^{\rm out}+\Theta_2^{\rm out})}],\end{aligned} \tag{72}$$

$$\langle\delta X_s^{\rm out}\delta X_s^{\rm out}\rangle_\omega=1+2\kappa_2[S_{34}+S_{43}+S_{33}e^{-i2\Theta_2^{\rm out}}+S_{44}e^{i2\Theta_2^{\rm out}}], \tag{73}$$

$$\langle\delta Y_m^{\rm out}\delta Y_m^{\rm out}\rangle_\omega=1+2\kappa_1[S_{12}+S_{21}-S_{11}e^{-i2\Theta_1^{\rm out}}-S_{22}e^{i2\Theta_1^{\rm out}}]. \tag{74}$$

IV. WORKING POINT FOR QND: THEORETICAL ANALYSIS

In this section we analyze, from a theoretical viewpoint, the configuration necessary to perform the QND measurement which was used in the experiment with cold atoms described in Sec. V. Rather then repeating a general analysis of the scheme, which was done in Ref. [12], we shall give some details on how the scheme can be realized and optimized in a real experiment by taking explicitly into account the constraints imposed by the optical cavity and by the atomic energy-level configuration.

A. Ghost transition scheme

We consider a configuration proposed by Gheri *et al.* [12], using a very intense signal field and a much weaker meter field driving the transitions 3-2 and 2-1 of the three-level atoms respectively. The strong signal has the double effect of (1) dressing the atomic transition 3-2 to which it is applied, and (2) transferring most of the atomic population to the ''bare'' ground level $|1\rangle$. The coupling between the two fields is achieved by tuning the meter in proximity of one of the two Rabi-split levels, originating from the bare excited state $|2\rangle$, whose separation depends upon the intensity of the strong field. In particular, under the proper conditions, a very efficient coupling between the signal intensity and the meter phase can be exploited for the QND measurement. Moreover, due to the large difference in strength between the meter and the signal field, nearly all the atomic population remains in the ground level $|1\rangle$ with the consequent advantage of keeping signal-absorption (and spontaneous emission) low. To a first approximation the signal is applied to an empty transition. This is why this configuration was called ''ghost transition scheme'' in Ref. [12].

In Figs. 2 and 3(a), we report two examples of the QND performances of the Λ scheme in the ghost transition configuration with parameters which are typical of our experiment. The QND criteria are calculated, at a fixed frequency of analysis, as a function of the meter atomic detuning which is scanned across the two Rabi-split levels, the meter being exactly tuned on one of the two dressed levels for $\Delta_1=$

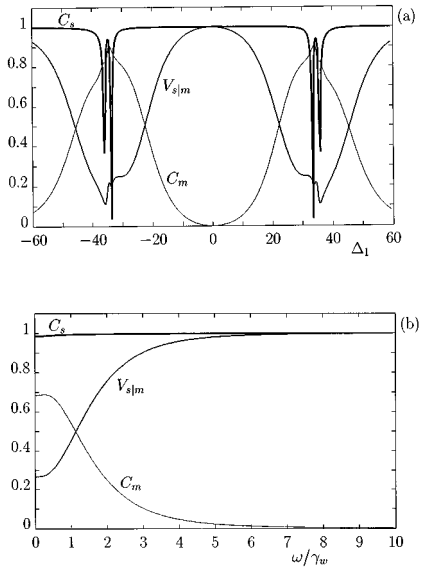

FIG. 2. (a) QND coefficients for $\omega=0$ as a function of the meter atomic detuning Δ_1. (b) QND coefficients for $\Delta_1=40.5$ as a function of the frequency of analysis ω/γ_w. Other parameters: $I_1=2$, $I_2=2450$, $\Delta_2=0$, $\Delta_1=40.5$, $C_1=135$, $C_2=90$, and $\kappa_1=\kappa_2=3\gamma_w$.

∓ 35 in both figures. Since the signal is taken at resonance with the atoms, the curves are symmetric with respect to $\Delta_1=0$. In these pictures, following the treatment in Ref. [12], we supposed both fields to be at resonance with the cavity, and we arbitrarily fixed the intracavity fields intensities I_1 and I_2 in a convenient range inspired from the experiment. The two figures differ in the value of I_1 which is four times larger in Fig. 3 than in Fig. 2. In both cases $I_2 \gg I_1$, as required by the ghost transition scheme. A convenient choice for the meter tuning is in proximity of the Rabi-split levels,

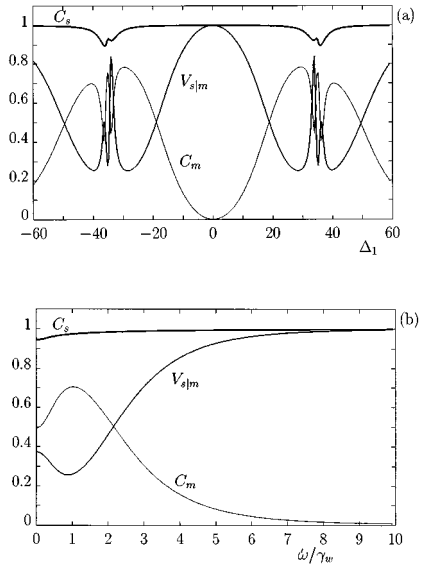

FIG. 3. (a) QND coefficients for $\omega=0.9\gamma_w$ as a function of the meter atomic detuning Δ_1. (b) QND coefficients for $\Delta_1=40.5$ as a function of the frequency of analysis ω/γ_w. Other parameters: $I_1=8$, $I_2=2450$, $\Delta_2=0$, $\Delta_1=40.5$, $C_1=135$, $C_2=90$, and $\kappa_1=\kappa_2=3\gamma_w$.

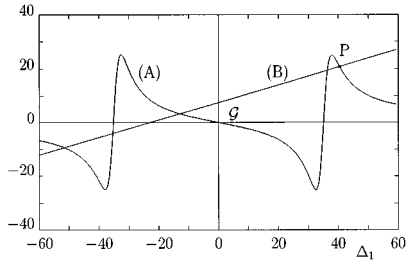

FIG. 4. Curve (A) [double-resonance condition (54)] and curve (B) [constraint relation (53) on the detunings], as functions of the meter atomic detuning Δ_1. Parameters: $I_1=8$, $I_2=2450$, $\Delta_2=0$, $C_1=135$, $C_2=90$, $\kappa_1=\kappa_2=3.05\gamma_w$, $\Delta_A=2276.6667$, $\Delta_C=753.9822$, and $\mathcal{G}=7.49$.

keeping, however, a certain detuning from the resonance with the Rabi levels in order to avoid strong meter absorption and consequent degradation of the ghost transition scheme [12].

In Figs. 2 and 3(b), we show the frequency dependence of the QND criteria for $\Delta_1=40.5$ in both cases. The frequency is normalized to γ_w, which in our case is about $\gamma_w/2\pi=3$ MHz. The case represented in Fig. 3(b), corresponding to $I_1=8$, $I_2=2450$, $\Delta_1=40.5$, and $\Delta_2=0$, seems more convenient from the experimental point of view, displaying the best QND performances ($C_s\simeq 0.9$, $C_m\simeq 0.7$, and $V_{s|m}\simeq 0.2$) around 3 MHz, which is above low-frequency technical noise.

B. Choice of the input fields and cavity parameters

By using our model, we wish to calculate the proper amplitudes and cavity detunings of the input fields, such that the favorable case represented in Fig. 3(b) is actually recovered in a realistic system.

We already know from Sec. III C that there is no complete freedom in choosing the cavity and the atomic detunings, and that Eqs. (53) and (54) should be fulfilled at the same time in order to have both fields at resonance in the cavity. We have represented these two conditions graphically in Fig. 4 as a function of the meter atomic detuning Δ_1. Curve (A) represents Eq. (54) when I_1, I_2, and Δ_2 are the same as in Fig. 3(b) (note that in the limit of strong signal and weak meter this curve represents as well the meter dispersion or phase shift). Curve (B) represents Eq. (53), with the parameters of our experiment and for a given value of the cavity length. At the intersection points between the two curves, both relations are satisfied, and Eqs. (48)–(51) can be used to calculate the exact values of the cavity detunings and input field amplitudes in order that the fields are set simultaneously at resonance in the cavity, with given values of I_1, I_2, and Δ_2 and with a value of Δ_1 corresponding to the intersection point we have chosen. In particular, for the intersection point P corresponding to $\Delta_1=40.5$, one recovers exactly the situation of Fig. 3(b).

The curves in Fig. 4 make it clear that, due to the constraint relation (53), the simultaneous resonance of the fields in the cavity can be achieved *only* for some particular sets of values of the atomic and cavity detunings. On the other hand, we have already pointed out that in many cases of interest the constraint coming from Eq. (53) can be overcome by

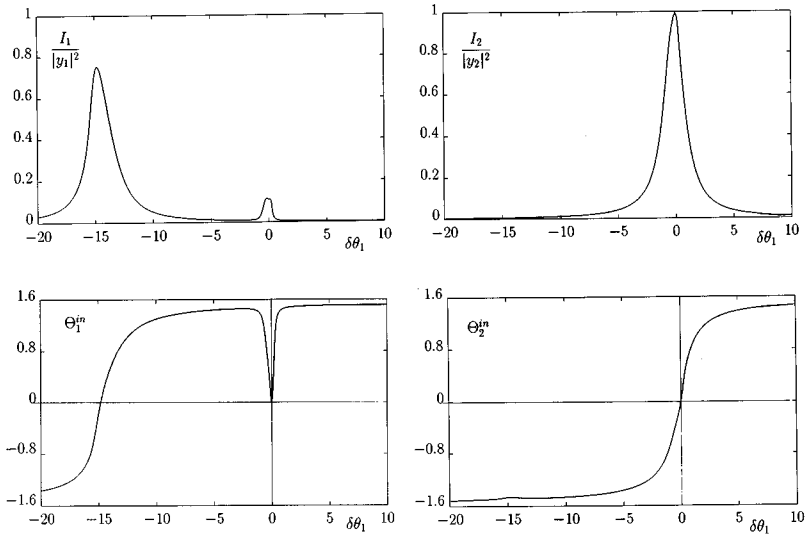

FIG. 5. Steady-state intensities (top) and phases (bottom) for the meter (left) and signal (right) fields as functions of the cavity detuning. The intensities I_1 and I_2 are normalized to the input intensities $|y_1|^2$ and $|y_2|^2$, respectively. Parameters: $y_1=8.6526$ $y_2=49.7193$, $\Delta_1=40.5$, $\Delta_2=0$, $C_1=135$, $C_2=90$, $\kappa_1=\kappa_2=3.05\gamma_w$, $\theta_{01}=20.9095$, $\theta_{02}=0.1360$, and $\mathcal{G}=7.49$.

adjusting the cavity length. In Fig. 4 these adjustments would correspond roughly to translate curve (B) thus ''choosing'' within some range the intersection point with curve (A). In a real experiment, in fact, what can be set precisely is not directly the cavity length but the $\mathcal{L}$-dependent quantity

$$\mathcal{G}=-\Delta_A\frac{\gamma_w}{\kappa_1}+\Delta_C, \tag{75}$$

accurately measured as the distance (in κ_1 units) between the empty-cavity resonances of the two fields when those are tuned exactly on the atomic resonances. This can be easily seen by setting $\Delta_1=\Delta_2=0$ in Eq. (53), which gives $\theta_1-(\kappa_2/\kappa_1)\theta_2=-\Delta_A(\gamma_w/\kappa_1)+\Delta_C$. In Fig. 4 (for $\Delta_2=0$) the quantity $\mathcal{G}$ is just the height of curve (B) at $\Delta_1=0$, equal in this case to $\mathcal{G}=7.5$.

C. Mean fields across the cavity scan

In order to understand more clearly how the double-resonance condition of the fields is achieved in the cavity, and to compare the theory with the experimental results, it is useful to plot the mean-field intensities of the signal and the meter when the cavity is scanned across the field resonance. In the experiment, this is done by sweeping in time the cavity length by a small amount $\pm\delta\mathcal{L}$ around the value $\mathcal{L}_0$ for which both fields are resonant in the cavity. To simulate the experimental procedure in our model, we decompose the cavity detunings θ_i $(i=1$ and $2)$ in Eqs. (31) and (32) as sums of two terms $\theta_i=\theta_{0i}+\delta\theta_i$, where θ_{0i} is a fixed initial cavity detuning, and $\delta\theta_i$ is a change in the detuning due to the variation of the cavity length. It is easy to verify that the $\delta\theta_i$ must satisfy

$$\delta\theta_1=\frac{\lambda_2 T_2}{\lambda_1 T_1}\,\delta\theta_2 \tag{76}$$

where λ_i $(i=1$ and $2)$ are the wavelengths of the modes, and T_i are the mirror transmission coefficients.[1] We plot an example in Fig. 5, where the input parameters are chosen as described in Sec. IV B. On the left we show the meter field intensity (upper curve) and phase (lower curve) across the cavity scan, and the same is shown on the right for the signal field. While the signal intensity curve displays the usual Lorenzian shape centered about the cavity resonance, the meter intensity curve displays two peaks: the ''proper'' resonance peak, shifted from its empty-cavity position $\delta\theta_1=-\theta_{01}$ by the linear and nonlinear dispersive responses of the atoms to the meter field alone; and a second peak, of necessarily nonlinear origin, induced in the meter at the signal resonance position for $\delta\theta_1=0$. Intuitively, the extra resonance in the meter field appears if the phase shift induced in the meter by the resonant signal equals the initial difference between the empty-cavity resonances of the two fields. In this very point of the cavity scan, where both fields are at resonance in the cavity (i.e., $\delta\theta_1=\delta\theta_2=0$), the configuration in Fig. 3(b) is in fact realized.

In Fig. 6 we show the corresponding QND coefficients calculated, at a fixed frequency of analysis $(\omega/2\pi=2.7$ MHz), along the cavity scan in the region of the induced peak where the fields are favorably coupled for QND. The best point of the scan is achieved at about $\delta\theta_1=0$, proving that the double-resonance condition of the two fields is actually the most favorable for the QND measurement. With this result in mind, parameters optimization, at least in principle, looks simpler: as a first step one adjusts the cavity

[1]When the cavity length is varied by a small amount $\mathcal{L}=\mathcal{L}_0+\delta\mathcal{L}$ from the definitions (22) and (21), and $\omega_{ci}=n_i 2\pi c/\mathcal{L}$ with $(i=1,2)$ and n_i an integer, one has $\theta_i=\theta_{0i}+\delta\theta_i$, with

$$\delta\theta_1=\frac{4\pi}{T_1}\frac{1}{\lambda_1}\,\delta\mathcal{L},\quad \delta\theta_2=\frac{4\pi}{T_2}\frac{1}{\lambda_2}\,\delta\mathcal{L},$$

from which Eq. (76) follows. In the case of our experiment, with $[(\lambda_2-\lambda_1)/\lambda_1]\simeq 10^{-5}$ and $T_1=T_2$, along the cavity scan we can approximate $\delta\theta_1=\delta\theta_2$.

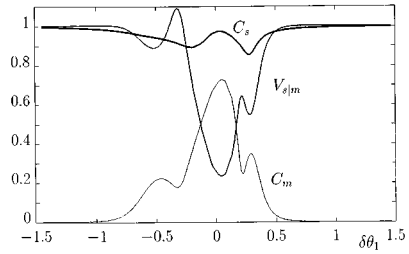

FIG. 6. QND coefficients for $\omega=0.9\gamma_w$ as a function of the cavity detuning in the region of the double-resonance position ($\delta\theta_1=0$). Parameters as in Fig. 5.

length as described in Sec. IV B. Then one adjusts the fields input powers, the laser frequencies, and the cavity detuning, in order to recover the favorable double-resonance configuration. If the result is not satisfactory, the whole process can be iteratively repeated for another cavity length.

V. EXPERIMENTAL SETUP

A. Magneto-optical trap

The MOT is built in a large ultrahigh vacuum (UHV) chamber, designed in order to set up the optical cavity directly around the cold atom cloud. The present setup uses ^{87}Rb atoms, with nuclear spin $I=\frac{3}{2}$, whose ground state $5S_{1/2}$ and excited states $5P_{3/2}$ ($D2$ line) and $5P_{1/2}$ ($D1$ line) are shown in Fig. 7 with their hyperfine sublevel structures. The trap is loaded by slowing down an atomic beam using the standard chirped-frequency technique [22]. The atomic beam part is separated from the UHV chamber containing the trap by a differential pumping aperture, which allows us to obtain a UHV pressure of a few 10^{-10} mbar in operating conditions. The central part of the chamber is about 80 cm far from the oven; at this point the atomic beam has a diameter of about 7 mm, and it is offset from the trap center by 1 cm. The ''slowing'' diode is swept on the quasiclosed $F=2$ to $F'=3$ transition on the $D2$ line at 780 nm (see Fig. 7), and a ''repumping'' diode is swept simultaneously on the $F=1$ to $F'=2$ transition. Both of them are free-running single-mode laser diodes (Hitachi HL 7851G and Mitsubishi ML 64110N-01). The powers sent onto the atoms are 30 (slowing) and 15 mW (repumping), with a 15-mm-diameter light beam whose part which could hit the trapped atomic cloud is carefully screened.

The atoms are trapped using a standard six-beams σ^+/σ^- MOT configuration [23]. A quadrupole magnetic field with a 8-G/cm gradient on axis is provided by two anti-Helmholtz

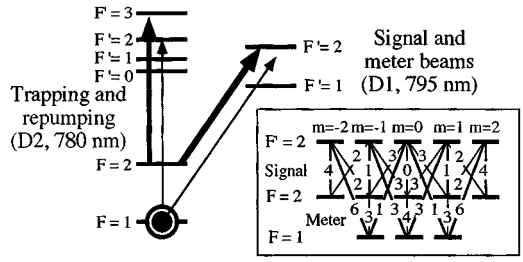

FIG. 7. Energy-level scheme of ^{87}Rb. The inset shows the relative strength for coupling the signal and meter beams which have linear orthogonal polarization.

coils spaced by about 50 mm, with a current of 20 A. The trapping lasers are two 100-mW laser diodes (SDL-5411-H2), injection locked to a master laser, which is a grating-extended laser diode locked to an appropriate saturated absorption line. An acousto-optical frequency shifter ensures an adjustable detuning. During the experiment, the trapping beams were detuned four natural linewidths to the red of the $F=2$ to $F'=3$ transition of the $D2$ line of rubidium atoms. The total power on the trap is typically three times 30 mW, with a beam diameter of 20 mm. As it is for the slowing process, a repumping laser diode (Mitsubishi ML 64110N-01) is locked on the $F=1$ to $F'=2$ transition, and pumps back into the trapping cycles the atoms which were lost in the $F=1$ ground state. This beam is superimposed on the trapping beams along two of the three axes. Its central part is screened thus forming a ''dark spot'' in the fields transverse profile [15], which is imaged at the trap location. In this way, the atoms in the trap cannot be repumped in the trapping cycle and, on average, about 90% of the population of the cloud is in the $F=1$ ground state. This point will be essential to allow simultaneous and continuous operation of the trap and QND experiments. The trap's absorption in the $F=1$ level is monitored using a weak probe beam. The trap fluorescence, mostly induced by the residual percentage of atoms in the $F=2$ state that are excited by the trapping beams, is measured by imaging it on a photodiode. The diameter of the trap is measured with a CCD camera, either in fluorescence ($F=2$) or in absorption ($F=1$); both measurements yield a value close to 3.5-mm full width at half maximum. The estimated values of the number N of atoms and density n in the $F=1$ dark state are $N=10^9$ and $n=5\times10^{10}$ atoms/cm^3.

B. Doubly resonant cavity

In order to obtain large effects at the quantum noise level, a vertical optical cavity is, set up inside the UHV chamber around the cold-atom cloud. The cavity mirrors have a 60 mm radius of curvature. Thanks to screws and piezoelectric transducers that can be handled from outside the UHV chamber, the cavity length is adjustable from 64 to 68 mm. The input-output cavity mirror has a 5% transmissivity. The upper mirror has a very low transmissivity (3×10^{-5}), and it is used to monitor the intracavity intensities while the cavity is scanned, thanks to two photomultipliers (see Fig. 8).

The level scheme used for the QND effect is shown in Fig. 7. The signal and the meter beams are tuned on the $D1$ line at 795 nm (whereas, as we already stated, the trapping and repumping beams are tuned on the $D2$ line at 780 nm). The signal is linearly polarized and tuned close to the $5S_{1/2}F=2$ to $5P_{1/2}F'=2$ transition with a typical input power of 15 μW. The meter beam, on the $F=1$ to $F'=2$ transition, is linearly polarized but orthogonally to the signal, and is tuned to the red with respect to the dressed levels due to the signal-atom coupling. Its typical input power is 250 nW. Both beams are emitted by two independent frequency-stabilized titanium-sapphire lasers. We carefully checked that they are shot noise limited both in intensity and phase in the frequency range of interest (2–20 MHz), which corresponds to our noise analysis frequency band since the linewidth of our cavity is $2\kappa/2\pi=18$ MHz. The two beams are carried onto the optical table by optical fibers which ensure

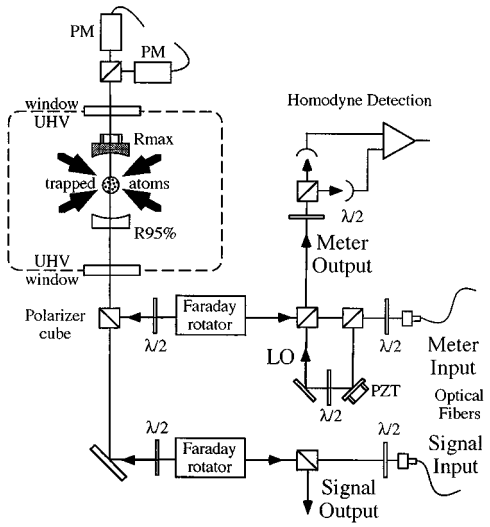

FIG. 8. Schematic view of the experimental setup. The input signal and meter beams are mode matched to an optical cavity surrounding the trapped atoms. Output beams are separated from the input ones using Faraday rotators. The signal beam is directly detected, while the meter beam undergoes a phase-sensitive homodyne detection.

very good spatial mode quality and best mechanical stability. They are mode matched to the optical cavity whose finesse is 125 with an efficiency above 99%. We also measured the optical transmission of the whole system, which is equal to 90% whereas the on-resonance losses of the cavity are negligibly small.

Note that the frequency difference between the signal and meter beam has to be close to the ground-state hyperfine splitting of ^{87}Rb, which is 6.83 GHz. Since both beams also have to be resonant on the cavity, this detuning has to be close to an integer number of the free spectral range (FSR) of the cavity. This is indeed the case when the cavity length is 66 mm, corresponding to a FSR of 2.27 GHz: the two beams are then shifted by three FSR's. As stated above, fine adjustment of the FSR value are still possible while the experiment is running. We note also that the two standing-wave patterns from the signal and meter beams have to be in phase at the atom location, so that the atoms see the appropriate Rabi frequencies from each beam. This is achieved by placing the trapped atoms cloud at one third of the cavity length, i.e., close to 22 mm from one mirror and 44 mm from the other one.

Finally, the output signal is directly detected by a high efficiency photodiode (Centronix BPX-65, quantum efficiency 92%), whereas the meter beam is detected by a phase-sensitive homodyne detection. The fringe visibility (homodyne efficiency) obtained by mode matching the local oscillator onto the meter beam output is 96%.

VI. EXPERIMENTAL RESULTS AND COMPARISON WITH THEORY

A. Mean-field configuration

The configuration we use to perform the QND measurement closely retraces what we have illustrated so far in theory. The strong signal is tuned slightly to the red of its atomic resonance, while the weak meter it is tuned to the red with respect to the lower of the two dressed levels originating from the excited state $|2\rangle$ due to the atom-signal coupling. In the experimental situation and in the notations of our model, the typical input powers of 15 μW for the signal and of 250 nW for the meter correspond to normalized amplitudes of the injected fields equal to $y_2=56$ and $y_1=7$, respectively, while the initial choice of the cavity length for which the two atomic frequencies are almost exactly three FSR's apart corresponds [see Eq. (75)] to $\mathcal{G}\simeq 0$.

After the cavity and input powers have been fixed, the atomic detunings are iteratively adjusted in order to optimize the QND coupling between the fields as follows. A weak intensity modulation at 5 MHz, about 20 dB above shot-noise level (SNL), is applied on the signal beam. When the two fields are coupled in the cavity, it is possible to read the same modulation in the phase of the meter beam by using a phase-sensitive homodyne detection technique. The detunings are adjusted by looking for the maximum transfer of the modulation from the signal onto the meter field and, simultaneously, for the minimum degradation of the signal. This is done while always scanning the cavity about the signal resonance, until a situation similar to the one depicted in Fig. 6 is achieved, where the maximum transfer along the cavity scan occurs in correspondence to the signal resonance. This situation is recovered in fact when both fields resonate at the same time in the cavity at the signal resonance position, as in Fig. 5.

In Fig. 9 we show an example of the mean-field configuration across the cavity scan when the parameters were optimized for the QND experiment. The experimental curves were taken, for the signal and meter intensities, both with and without the trapping beams, thus ''switching on'' and ''switching off'' the nonlinearity. The solid line, superimposed on the ''noisy'' experimental curves, shows the *theoretical* curves obtained for $y_2=42.120$, $y_1=8.768$, $\Delta_2=2$, $\Delta_1=41.3$, $\theta_{01}=0.169$, $\theta_{01}=11.207$, $C_2=135$, $C_1=90$, $\kappa_1=\kappa_2=9.034$, and $\mathcal{G}=-2.01$. The signal curves are shown upside down, and each curved is normalized to the corresponding intensity at resonance in the empty cavity. In Fig. 10 we again show the meter field in the presence of the atoms (intensity and phase across the cavity scan) to point out that the ''nonlinear'' meter peak at the signal resonance position $\delta\theta_1=0$ is actually an extra resonance for the meter field. This very point is the working point for the experiment. Here the cavity scan is stopped and the QND coefficients are measured.

B. QND coefficients

Typical experimental results for the QND coupling between the fields in the case of the mean-field configuration in Fig. 9 are shown in Fig. 11. The lower trace (a) shows the SNL, and the modulation of the output signal beam, taken off cavity resonance without the atoms; the width of the modulation peak is 100 kHz. Over this trace are also shown as dots the SNL and modulation of the output signal beam, taken while the cavity is stopped at resonance in the presence of the atoms (operating conditions). There is clearly neither attenuation nor a change in the noise of the signal beam. The measured nondemolition coefficient T_s is therefore limited

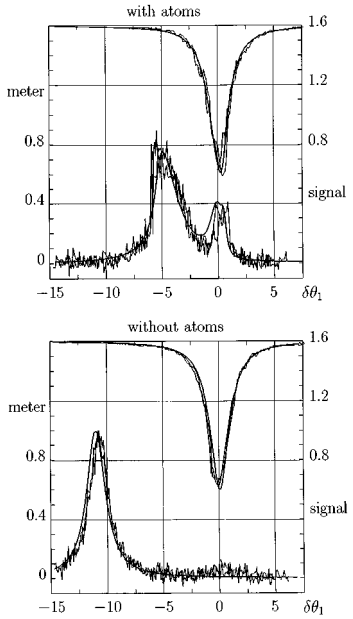

FIG. 9. Normalized intensities of the meter and signal (up side down) as functions of the cavity detuning. The curves were taken both in presence and in absence of the atomic medium. The thin continuous line is the theoretical curve, while the noisy lines are experimental curves. The little bump which appears on the meter curve without the atoms at the signal position is due to a small imperfection in the optics separating the two beams in the monitoring channel. The parameters for the theoretical curves are $y_1=8.768$, $y_2=42.120$, $\Delta_1=41.3$, $\Delta_2=2$, $C_1=135$, $C_2=90$ ($C_1=C_2=0$ for the curves without atoms), $\kappa_1=\kappa_2=3.01\gamma_w$, $\theta_{01}=11.207$, $\theta_{02}=0.169$, and $\mathcal{G}=-2.01$.

only by the passive optical transmission of the system, which relates the output signal without atoms to the input one, i.e., $T_s^{(\mathrm{meas})}=0.90(-0.5\ \mathrm{dB})$. From T_s and from the lower trace in Fig. 11, one obtains the input beam signal to noise ratio, which is 23.8 dB. The upper trace (b) is the phase-dependent noise and modulation of the output meter beam, taken in operating conditions while scanning the phase of the homodyne detection. The SNL of the meter beam was electronically set at the same level as the one of the signal beam. The upper envelope of the fringes gives the meter phase information, and yields the output meter signal-to-noise ratio, which is equal to 21.9 dB. The measurement transfer coefficient is thus -1.9 dB, or $T_m^{(\mathrm{meas})}=0.65$. Finally, the conditional variance is obtained by recombining the output signal and meter

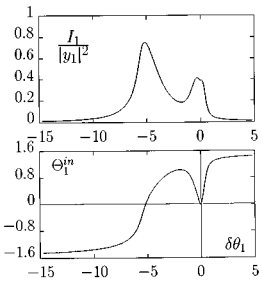

FIG. 10. Meter intensity (top) and phase (bottom) as a function of the cavity detuning, in presence of the atoms. The parameters are as in Fig. 9.

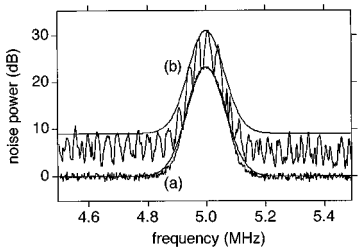

FIG. 11. Measurement of the transfer coefficient T_m. Curve (a), normalized to the SNL, corresponds to the output signal, modeled by a Gaussian peak (dash-dotted line). Two curves are actually displayed, and show no observable difference: one taken off resonance without the atoms (line) and one taken on operating conditions (dots). Curve (b) is the outcoming meter, also taken on operating conditions, and modulated by scanning the phase of the homodyne detection. The upper envelope is fitted by a Gaussian peak of same width as in curve (a). The signal-to-noise ratios are obtained as the differences (in dB) between the fitted peaks and the flat backgrounds.

photocurrents while scanning the phase of the homodyne detection. We show the results in Fig. 12. In correspondence to the right phase of the local oscillator picking up the *phase quadrature* of the meter field, the recombined noise reaches a minimum value 3.5 dB below the SNL, which gives a conditional variance $V_{s|m}^{(\mathrm{meas})}=0.45$. Estimated uncertainties on $T_s^{(\mathrm{meas})}$, $T_m^{(\mathrm{meas})}$, and $V_{s|m}^{(\mathrm{meas})}$ are ± 0.05.

In order to compare the experimentally measured values of the QND coefficients with the theory, it is necessary to take into account some small corrections due to optical losses and nonunity efficiencies. The quantum efficiencies on the two channels are

$$\eta_s=\alpha_s^{\mathrm{res}}\beta_s^{\mathrm{prop}} \tag{77}$$

for the signal beam, and

$$\eta_m=\alpha_m^{\mathrm{res}}\beta_m^{\mathrm{prop}}\mathcal{V}^2\epsilon_m^{\mathrm{det}} \tag{78}$$

for the meter beam, where α_s^{res} and α_m^{res} are the cavity losses at resonance for the signal beam and the meter beam, respectively; β_s^{prop} and β_m^{prop} are the optical losses on propagation for the signal beam and the meter beam, respectively, $\mathcal{V}$ is

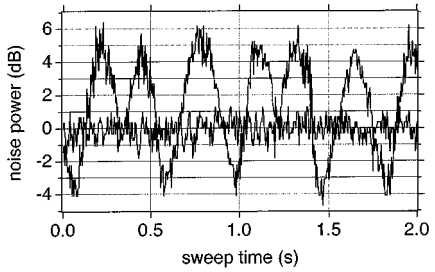

FIG. 12. Measurement of the conditional variance. The dotted line is the signal beam shot noise level at a noise analysis frequency of 4.6 MHz. The full line is the noise from the recombined signal and meter photocurrents, recorded as the phase of the homodyne detection is scanned. The conditional variance appears as the minimum noise level of this curve.

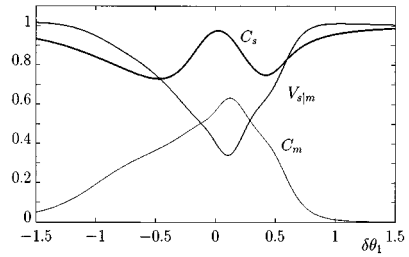

FIG. 13. QND coefficients for $\omega = 1.533\gamma_w$ as a function of the cavity detuning in the region of the double-resonance position ($\delta\theta_1 = 0$). The parameters are as in Fig. 9.

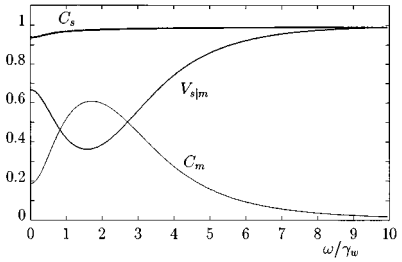

FIG. 14. QND coefficients in the best point of the scan ($\delta\theta_1 = 0.11$) as a function of the frequency of analysis. The parameters are as in Fig. 9.

the fringe visibility of the homodyne detection, and $\epsilon_m^{\rm det}$ is the meter detector quantum efficiency.

With our setup (Sec. V), we have

$$\alpha_s^{\rm res} = \alpha_m^{\rm res} = 1, \quad \beta_s^{\rm prop} = \beta_m^{\rm prop} = 0.90, \quad \mathcal{V} = 0.96, \quad \epsilon_m^{\rm det} = 0.92, \tag{79}$$

which implies $\eta_s = 0.9$ and $\eta_m = 0.76$. The QND coefficients, due *only* to the interaction with the nonlinear medium which are used in the theoretical model (where experimental imperfections are not taken into account), are then related to the measured ones through η_s and η_m. For the coefficient T_s one has simply

$$T_s^{(\rm meas)} = \eta_s T_s . \tag{80}$$

To evaluate T_m, one has to take into account the fact that, after the interaction, the meter has a strong phase noise $\langle \delta\tilde{Y}_m^{\rm out}(\omega)^2 \rangle$. In the limit of high gains, one can show that [14]

$$T_m^{(\rm meas)} = B_m T_m \quad \text{where} \quad B_m = \frac{\eta_m \langle \delta\tilde{Y}_m^{\rm out}(\omega)^2 \rangle}{\eta_m \langle \delta\tilde{Y}_m^{\rm out}(\omega)^2 \rangle + 1 - \eta_m}. \tag{81}$$

For $\langle \delta\tilde{Y}_m^{\rm out}(\omega)^2 \rangle \gg 1$ [like in our case in which $\langle \delta\tilde{Y}_m^{\rm out}(\omega)^2 \rangle = 7.9$], one obtains

$$B_m = 1 - \frac{1 - \eta_m}{\eta_m \langle \delta\tilde{Y}_m^{\rm out}(\omega)^2 \rangle}. \tag{82}$$

For the conditional variance, one can deduce

$$1 - V_{s|m}^{(\rm meas)} = B_m \eta_s (1 - V_{s|m}). \tag{83}$$

By using Eqs. (80)–(83), where we substitute the numerical values (79) for our setup and the measured values for the QND coefficients, we can work out the experimental values for the QND coefficients, corrected for the optical losses. One obtains $T_m = 0.67$, $T_s = 1$, and $V_{s|m} = 0.37$, again with an uncertainty estimated to be about ± 0.05 on each coefficient.

We can directly compare these results with the theoretical prediction, in Fig. 13, for the QND coefficients calculated at $\omega/2\pi = 4.6$ MHz along the cavity scan in the region of the double-resonant point. At the best point of the scan one has $T_m = 0.60$, $T_s = 0.97$, and $V_{s|m} = 0.36$, which is in good agreement with the experiment. In Fig. 14 we finally show the frequency dependence of the QND coefficients at the best point of the scan. As confirmed by the experiment, the quantum correlations display a significant frequency dependence within the frequency band selected by the cavity. The best values are reached around 5 MHz, once more corresponding to the experimental observations.

C. Remarks

As we have shown, the agreement found between the experimental results and the theoretical analysis performed with a three-level model for the atoms is remarkable. The model is able to reproduce and interpret the main experimental results which concern, on the one hand, the steady-state curves of the field intensities across the cavity scan, and, on the other hand, the quantum correlations between the fields in the best configuration for QND identified as the point of the cavity scan where the two fields resonate simultaneously. Nevertheless it is needless to remark that the distance between the three-level model presented in this paper (Sec. III) and the complex situation of a real experiment remains very large. At least two major omissions in the model can be identified.

The first of these is that the restriction to a purely three-level system does not take into account the actual multilevel structure of the transitions used for the two-beam coupling. A schematic view of the involved Zeeman sublevels is represented in the inset of Fig. 7, where we also show the relative importance of the Clebsch-Gordan coefficients for the different transitions. The chance to represent this complicated situation successfully as a simple lambda scheme comes from the fact that most of the contribution to the coupling is given by the lambda schemes (the outermost in the figure) which have the largest Clebsch-Gordon coefficients, and it is indeed by considering these most contributing transitions that we have chosen to set the ratio $C_1/C_2 = 1.5$ in our model to fit the experimental curves.

The second major fault of the model is that, by describing the fields in the cavity as plane waves, it neglects the Gaussian transverse shape of the beams as well as their standing-wave longitudinal structure in the cavity. These spatial gradients in the intensity profile of the waves, and especially the standing-wave structure in the cavity, give rise to optical potentials whose depth can easily be of the same order of magnitude of the small kinetic energy of the cold atoms, thus sizably affecting their external degrees of freedom. Preliminary experiments performed with our setup on one-photon optical bistability showed with some evidence that optical forces due to a strong standing wave in the cavity can have

macroscopic effects on the nonlinearity of the cold atoms, changing the effective cooperativeness of the system in a detuning and intensity-dependent way. The major practical conclusion of this preliminary study was that it is preferable to use red (positive) detuning for the fields, a condition in which the effective cooperatively of the system can be increased sizably with respect to the opposite case of blue (negative) detuning. An attempt at an explanation for this was made on the basis of a very simple model based on the dipole force that would attract cold atoms in the high-intensity regions of the field for red detuning, and repulse them for blue detuning [24]. A more complex situation involving two different light fields was analyzed theoretically very recently [25].

In this view, a too-strict correspondence between the parameters introduced in the model (especially the cooperativity parameters and the input fields amplitudes) and their experimental counterparts loses sense. Instead we are naturally led to consider the parameters of our theoretical model as ''averages'' over more complex phenomena that take place in the real experiment. The very fact that such effective parameters can be defined, and used to obtain a very good description of the results, is actually a good proof of the robustness of the three-level model in our experimental configuration.

VII. CONCLUSIONS

We presented the results of a recent QND experiment performed with cold trapped rubidium atoms [10], and their interpretation on the basis of a theoretical model for three-level atoms in a cavity. By studying in detail the steady-state configurations allowed by the system and the quantum behavior of the fields, we showed by theory and experiment, how a ghost transition configuration for performing QND measurements with atomic $\chi^{(3)}$ nonlinearity can be successfully implemented and optimized using cold atoms. The experimental results are the best obtained so far for a single back-action-evading measurement, and the agreement between theory and experiment is remarkable.

ACKNOWLEDGMENTS

This work was carried out with the support of the European HCM network ''Non-Classical Light.'' One of us, A. S., would like to thank Professor L. Lugiato and Professor G. Strini for fruitful discussions and quite useful advice. One of us, K. W., acknowledges financial support from ICTP Programme, Trieste, Italy and the National Natural Science Foundation of China.

APPENDIX

Here we report the elements of the diffusion matrix D_N, expressed in terms of the normalized variables:

$$[x_1, x_1^*, x_2, x_2^*, v, v^*, w, w^*, z, z^*, m, n,]:$$

$$(D_N)_{6,6} = -\frac{2\gamma_w}{N} x_1 v^*,$$

$$(D_N)_{6,8} = -\frac{\gamma_w}{N} (x_1 \omega^* + x_2 v^*),$$

$$(D_N)_{6,10} = -\frac{\gamma_w}{N} x_1 z^*,$$

$$(D_N)_{8,8} = -\frac{2\gamma_w}{N} x_2 w^*,$$

$$(D_N)_{8,10} = \frac{\gamma_w}{N} [x_2 z^* + x_1 (n-m)],$$

$$(D_N)_{8,11} = \frac{\gamma_w}{N} x_1 z,$$

$$(D_N)_{8,12} = -\frac{\gamma_w}{N} x_1 z,$$

$$(D_N)_{9,10} = \frac{\gamma_w/2}{N} [x_1 (v + v^*)] + \frac{\gamma_1}{N} [1/3\eta(1-m-n)],$$

$$(D_N)_{10,11} = -\frac{\gamma_w/2}{N} \eta (x_1 w + x_2 v^*),$$

$$(D_N)_{10,12} = -\frac{\gamma_w}{N} (x_1 w + x_2 v^*),$$

$$(D_N)_{11,11} = \frac{2\gamma_w}{N} \left[x_1 (v + v^*) + \frac{x_2}{4} (w + w^*) \right] + \frac{\gamma_1}{N} \left[\frac{4}{3} (1 + \eta/4)(1-m-n) \right],$$

$$(D_N)_{11,12} = \frac{\gamma_w}{N} [x_1 (v + v^*) + x_2 (w + w^*)] + \frac{\gamma_1}{N} \left[\frac{2}{3} (1+\eta)(1-m-n) \right],$$

$$(D_N)_{12,12} = \frac{2\gamma_w}{N} \left[\frac{x_1}{4} (v + v^*) + x_2 (w + w^*) \right] + \frac{\gamma_1}{N} \left[\frac{4}{3} \left(\frac{1}{4} + \eta \right) (1-m-n) \right],$$

plus the ones obtained by conjugation and index permutation from the terms above (we recall that D_N is symmetrical).

[1] V. B. Braginsky and Yu. I. Vorontsov, Usp. Fiz. Nauk. **114**, 41 (1974) [Sov. Phys. Usp. **17**, 644 (1975)]; V. B. Braginsky, Yu. I. Vorontsov, and F. Ya. Khalili, Zh. Eksp. Teor. Fiz. **73**, 1340 (1975) [Sov. Phys. JETP **46**, 705 (1977)].

[2] K. S. Thorne, R. W. P. Drever, C. M. Caves, M. Zimmerman, and V. D. Sandberg, Phys. Rev. Lett. **40**, 667 (1978).

[3] G. J. Milburn and D. F. Walls, Phys. Rev. A **28**, 2065 (1983); N. Imoto, H. A. Haus, and Y. Yamamoto, *ibid.* **32**, 2287 (1985); B. Yurke, J. Opt. Soc. Am. B **2**, 732 (1985).

[4] M. D. Levenson, R. M. Shelby, M. Reid, and D. F. Walls, Phys. Rev. Lett. **57**, 2473 (1986).

[5] A. LaPorta, R. E. Slusher, and B. Yurke, Phys. Rev. Lett. **62**, 28 (1989).

[6] P. Grangier, J. F. Roch, and G. Roger, Phys. Rev. Lett. **66**, 1418 (1991).

[7] S. R. Friberg, S. Machida, and Y. Yamamoto, Phys. Rev. Lett. **69**, 3165 (1992).

[8] J. Ph. Poizat and P. Grangier, Phys. Rev. Lett. **70**, 271 (1993).

[9] K. Bencheikh, J. A. Levenson, Ph. Grangier, and O. Lopez, Phys. Rev. Lett. **75**, 3422 (1995).

[10] J.-F. Roch, K. Vigneron, P. Grelu, A. Sinatra, J-P. Poizat, and P. Grangier, Phys. Rev. Lett. **78**, 634 (1997).

[11] M. D. Levenson, M. J. Holland, D. F. Walls, P. J. Manson, P. T. H. Fisk, and H. A. Bachor, Phys. Rev. A **44**, 2023 (1991).

[12] K. Gheri, P. Grangier, J. P. Poizat, and D. Walls, Phys. Rev. A **46**, 4276 (1992).

[13] A. Lambrecht, T. Coudreau, A. M. Steinberg, and E. Giacobino, Europhys. Lett. **36**, 93 (1996).

[14] J.-Ph. Poizat and P. Grangier, in *ICONO '95; Coherent Phenomena and Amplification Without Inversion*, edited by A. V. Andreev, O. Kocharovskaya, and P. Mandel [Proc. SPIE **2798**, 260 (1996)].

[15] W. Ketterle, K. Davis, M. Joffe, A. Martin, and D. Pritchard, Phys. Rev. Lett. **70**, 2253 (1993).

[16] M. J. Holland, M. J. Collett, D. F. Walls, and M. D. Levenson, Phys. Rev. A **42**, 2995 (1990).

[17] J. P. Poizat, J. F. Roch, and P. Grangier, Ann. Phys. (Paris) **19**, 256 (1994).

[18] L. A. Lugiato, *Progress in Optics XXI*, edited by E. Wolf (North-Holland, Amsterdam, 1977), p. 71.

[19] C. W. Gardiner and M. J. Collett, Phys. Rev. A **31**, 3761 (1985).

[20] A. Sinatra, Ph.D. thesis, Università di Milano, 1997 (unpublished).

[21] J. M. Courty, P. Grangier, L. Hilico, and S. Reynaud, Opt. Commun. **83**, 251 (1991).

[22] B. Sheehy, S. Q. Shang, R. Watts, S. Hatamian, and H. Metcalf, J. Opt. Soc. Am. B **6**, 2165 (1989).

[23] E. Raab, M. Prentiss, A. Cable, S. Chu, and D. Pritchard, Phys. Rev. Lett. **59**, 2631 (1987).

[24] A. Sinatra, K. Vigneron, P. Grelu, J.-Ph. Poizat, J.-F. Roch, and P. Grangier, 1996 European Quantum Electronic Conference, Hamburg (1996), IEEE Catalog No. 96TH8162, Library of Congress: 95-82410.

[25] W. Alge, K. Ellinger, H. Stecher, K. M. Gheri, and H. Ritsch, Europhys. Lett. **39**, 491 (1997).